Calibration of MAJIS (Moons And Jupiter Imaging Spectrometer): II. Spatial calibration

Gianrico Filacchione, Giuseppe Piccioni, Simone De Angelis, Stefania Stefani, and Federico Tosi
INAF-IAPS, Istituto di Astrofisica e Planetologia Spaziali, via del Fosso del Cavaliere, 100, 00133, Rome, Italy

Paolo Haffoud, Francois Poulet, Yves Langevin, John Carter, Cydalise Dumesnil, and Mathieu Vincendon
Institut d'Astrophysique Spatial, CNRS-Université Paris-Saclay, Orsay, 91400, France

Leonardo Tommasi, Alessandra Barbis, and Irene Guerri
Leonardo Company, via delle Officine Galileo, 1, Campi Bisenzio, Florence, 50013, Italy

Cedric Pilorget
Institut d'Astrophysique Spatiale, CNRS-Universite Paris-Saclay, Orsay, 91400, France; Institut Universitaire de France, Paris, France.

Sebastien Rodriguez
Institut de Physique du Globe de Paris, CNRS-Université Paris-Cité, Paris, 75005, France
(*gianrico.filacchione@inaf.it)
(Dated: March 30, 2024)

MAJIS, the Moons and Jupiter Imaging Spectrometer, is one of the scientific payloads aboard ESA's JUICE (Jupiter Icy Moons Explorer) mission. The instrument underwent a comprehensive characterization and calibration campaign before integration on the spacecraft. In this work, we report on the measurements of the instrumental spatial responses including the slit and pixel functions, the knife edge function, the ensquared energy, and the keystone aberration. The measurements were repeated in several positions of the Filed of View (FoV) and within the range of MAJIS temperatures during science observations. The goal was to characterize the instrument's response in a wide set of conditions and at different VIS-IR wavelengths. The experimental setups employed to perform the calibrations are described in detail, and the methodology applied to derive the instrumental spatial responses is discussed. After launch, minor changes of the instrument response and the coalignment between the two spectral channels were identified by comparing on-ground data with the first in-flight data returned by MAJIS.

I. INTRODUCTION

MAJIS (Moons and Jupiter Imaging Spectrometer) is the advanced VIS-IR hyperspectral imager onboard the ESA JUICE spacecraft launched on April 14 2023 aiming to explore the Jupiter atmosphere and its icy moons, in particular Ganymede. The instrument is realized by a French-Italian team under IAS-Orsay leadership [12]: the design and realization of the main electronics unit and the procurement of the two focal plane arrays is under French responsibility. The Optical Head (OH) design, integration, and test are provided by Italy.

The MAJIS optical design is based on a Three Mirrors Anastigmatic (TMA) telescope focusing on a single entrance slit (width 38 μm). By means of a dichroic filter, the diffracted beam is separated in-field between two spectral channels, both telecentric: the VISNIR camera-spectrometer resolving the 0.5-2.35 μm spectral range with a sampling of $\approx$3.65 nm/band, and the IR camera-spectrometer operating between 2.25-5.54 μm with a sampling of 6.5 nm/band. The camera-spectrometers employ collimating and focusing lenses to disperse the beams on flat gratings and to collect the diffracted light across 2D HgCdTe CMOS detectors. Two Teledyne H1RG detectors, with a format of 1024$\times$1024 pixels, 18 μm pixel pitch (physical pixel px_{ph}) are employed as focal planes. The two detectors share similar readout architectures with different compositions of the sensitive layer and are optimized for their respective spectral range and cut off-cut on wavelengths [4, 7, 11]. The MAJIS telescope has a Field of View (FOV) of 3.4°, spatially resolved with an IFOV of 150 μrad each (400 MAJIS pixels binning 2$\times$2 physical pixels). The spectral range of each channel is resolved by 504 bands. Thanks to a flat mirror mounted on a steerable mechanism placed at the telescope's entrance it is possible to operate the instrument in pushbroom, scan and motion-compensation modes resulting in high operational flexibility. The MAJIS optical design and analysis is detailed in [6]. Additional features of the MAJIS instrument are the presence 1) of a shutter, placed at the entrance slit of the spectrometers which can be commanded in closed position to acquire dark current and spectrometer's internal background signal, and 2) of the Internal Calibration Unit (ICU) housed on the side of the telescope's entrance baffle and designed to inject reproducible VIS-IR signals into the optical path to monitor the instrument's performances during the entire lifetime of the instrument [14]. The optics and detectors are mounted on an bench within the Optical Head (OH) thermomechanical structure designed and manufactured by Leonardo (Campi Bisenzio, Florence, Italy). It also includes two passive radiators necessary to cool down the optics and the VISNIR detector at $\leq$130 K and the IR detector at $\leq$90 K. The OH is maintained mechanically aligned with the spacecraft's nadir pointing axis by means of three isostatic bipods. The bipods' design and the use of thermal washers allows to isolate the OH from the conductive thermal load from the spacecraft bus. Additional radiative thermal exchanges are minimized by wrapping the entire OH with Multi-Layer Insulation (MLI) with the exception of the radiators' surfaces and the telescope's entrance baffle. The instrument is designed to operate and survive in the harsh radiation environment of the Jupiter magnetosphere by adopting rad-hard optical and electronics components and by adding distributed and localized shielding to protect the most sensitive elements, like detectors and electronics unit.

The instrument is managed by a Main Electronics (ME) Unit designed and procured by IAS-Orsay, France. The ME generates the science data, engineering telemetry and power links with the spacecraft, and it distributes power to the different instrument subsystems. The onboard software manages the acquisition and timing of the science and telemetry data, their despiking, compression and formatting [9]. A dedicated Auxiliary board by Leonardo Company commands the steerable mirror motor, the shutter mechanism, and the internal calibration unit sources.

Due to the complexity of the instrument, several activities have been performed to characterize the single subsystems and to calibrate the payload in different phases of the integration. In a series of papers we report about the experimental setups used to calibrate the MAJIS instrument before launch [16], the results of the spectral calibration [8], the derivation of the radiometric calibration [10], the characterization of the Internal Calibration Unit [14] and the measurements of several spectral targets, e.g., mineral samples and calibration targets, used to test the instrumental performances [13].

In this paper we will focus specifically on the calibration of the spatial response of the two spectral channels which are then compared with the instrument's scientific requirements. In section II we present the Pixel and Slit Function theory for evaluating the spatial resolution. The calibration setups in Leonardo and in IAS used to perform spatial measurements across the VISNIR and IR spectral range are presented in section II B. The characterization of the slit, pixel, and edge functions as a function of different positions within the FoV and at different wavelengths is detailed in section III. This section also discusses the coalignment between the VISNIR and IR spectral channels before the launch. The Ensquared Energy for the VISNIR channel is addressed in section IV, while the investigation of the instrumental spatial response stability with temperature is discussed in section V. Section VI reports the measurements and analyses performed to evaluate the keystone distortion on the two spectral channels. The stability of the spatial response, as measured during the onground calibration campaign, is checked on the first data returned by MAJIS after the launch. A description of the spatial response changes that occurred during the launch is given in section VII. The conclusions (section VIII) summarize the MAJIS spatial response parameters across the range of temperatures, wavelengths, and positions of the FoV as explored during the ground and flight calibration phases.

II. SPATIAL RESPONSE FUNCTIONS

A. Goals and methods

The spatial response of an imaging spectrometer can be characterized through the measurement of the Pixel and Slit functions which respectively correspond to the instrumental resolution along and across the spectrometer's slit directions [15]. The Pixel Function, $F_P(s)$, on a pixel located at a given location (s) along the slit direction, is given by the convolution of the unitary step function, $V(s)$, representing the physical pixel spatial response, and the instrument response, INST(s), along the slit:

$$F_P(s) = V(s) \bigotimes INST(s) \tag{1}$$

Similarly, the Slit Function, $F_S(l)$, for a pixel located along the scan direction at line (l), can be expressed as the convolution of the unitary step function $U(l)$, corresponding to the slit spatial response of the spectrometer, and the telescope response TEL(l) along the scan direction:

$$F_S(l) = U(l) \bigotimes TEL(l) \tag{2}$$

The instrument spatial response along the slit is therefore defined by the Full-Width at Half-Maximum (FWHM) of the pixel function profile, while the response across the slit is the FWHM of the slit function. It is important to distinguish the difference between the spatial response width and the instrumental Instantaneous Field of View (IFOV). While the former is related to the instrument spatial resolution, e.g. the minimum angle under which the instrument is capable of resolving two adjacent point sources, the latter describes the spatial sampling (in radians) of an image, and it is a function of the pixel's size (d_{px}) and the instrument focal length (F) through the relation:

$$IFOV = 2\, arctg\left(\frac{d_{px}}{2F}\right) \tag{3}$$

Ideal imaging systems would have unitary step function responses, e.g. would be able to collect all photons coming from a point source on a given pixel without spreading them across neighboring pixels. For real optical systems there is a broadening of the point source signal. Therefore, the spatial response function must be characterized across a wide set of instrumental parameters. So as to achieve the science goals of MAJIS, a requirement (FWHM $\leq$ 225 μrad) has been defined for the spatial response, corresponding to a spatial FWHM $\leq$ 54 μm across the detector, which is 1.5 times the nominal IFOV (150 μrad or 36 μm, nominal pixel size px_{nom}). For the sake of completeness, we recall that this value is derived from Eq. 3, in which the MAJIS equivalent focal length (F) is 240 mm. The instrument's pupil diameter is 75 mm and the f/#=3.2 [6].

The MAJIS Pixel and Slit functions have been characterized from multiple acquisitions of a test slit image scanning along and across the MAJIS slit direction. For each tested pixel, we measured the variation of the test slit signal during the scan and the FWHM was derived from the best gaussian fit of these variations. The scheme of the two spatial scans is shown in Fig. 1. Since the MAJIS optics is designed to observe targets at infinite distances and is not equipped with a focusing mechanism able to resolve objects at finite distances, a collimator is used to collimate the beam from the test slit. The same scheme has been implemented for characterizing the spatial response of previously flown imaging spectrometers such as, VIRTIS on Rosetta [2], JIRAM on Juno [1], and SIMBIO-SYS/VIHI on BepiColombo [5]. The description of the experimental setup is given in the next section.

B. Calibration setups

1. *Calibration setup at Leonardo*

In this section we describe the Optical Ground Support Equipment (OGSE) utilized to carry out the spatial calibrations in Leonardo (Campi Bisenzio, Florence, Italy). Leonardo (hereafter LDO) is the prime industrial partner for the design, manufacturing, integration and testing of the MAJIS optical head. A scheme of the OGSE setup is shown in Fig. 2 and further described in [3]. An Off-axis (by an angle 9.53°) parabola with a diameter of 20.3 cm and a focal length F_{Coll}=1538 mm is employed as a collimator whose focal plane is matched to the test slit. The test slit has a physical clear aperture of 0.075 $\times$ 3 mm. Given the Magnification Ratio of the setup (MR=F_{MAJIS}/F_{Coll}=0.156), the slit image seen by MAJIS corresponds to a size of 12 μm $\times$ 468 μm = 0.33 pixel $\times$ 13 nominal pixels on the MAJIS focal plane. The test slit axis can be oriented along the vertical or horizontal directions depending on the measurement to be performed (see Fig. 1). The test slit is mounted on a circular mechanical mount whose center corresponds to the optical axis so as to set it in either vertical or horizontal directions. As the MAJIS slit is oriented along the vertical direction during the measurements, the slit function is measured when the test slit is placed in the vertical

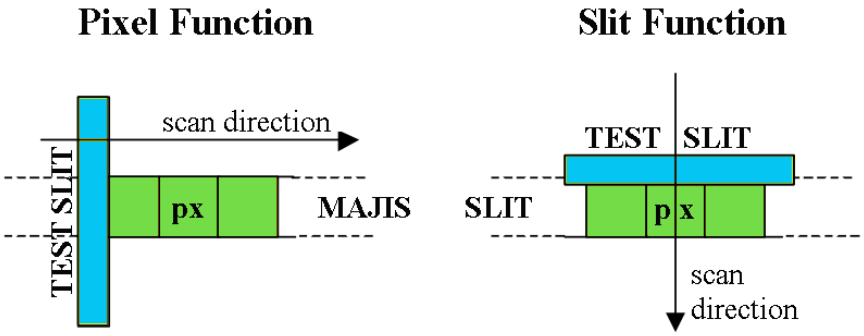

FIG. 1. Pixel (left) and Slit (right) functions conceptual scheme: the signal of the illuminated test slit is acquired while performing a spatial scan above a test pixel (px). The test slit is oriented perpendicular to the MAJIS slit for determining the Pixel function and parallel to the MAJIS slit for determining the slit function.

direction and the pixel function is measured when the test slit is oriented in the horizontal direction. The test slit can be moved along the horizontal or vertical directions by a 2 axes motorized linear stage (Micronix PPS-60-41310) so as to perform the spatial scans within the instrument's FOV with an accuracy position of ± 1 μm in the OGSE focal plane. The zero order of a monochromator (ACTON RESEARCH SP-2355i) is employed as a light source. This solution has been implemented to perform spatial and spectral characterizations by adopting a common setup without the necessity to introduce significant changes in the OGSE configuration. The spatial scan measurements were repeated two times: the first time the monochromator is equipped with a QTH source and a diffraction grating optimized to maximize the signal in the VISNIR spectral range; a second scan is made by replacing the QTH source with an IR emitter (model 6363 by Oriel) and changing the grating to reach high efficiency at IR wavelengths. In both cases the input and output slits of the monochromator are set with an aperture of 2 mm. The monochromator's exit slit is oriented along the vertical axis and the zero order light beam at the exit of the monochromator is aligned with the test slit. Since the physical width of the test slit (75 μm) is much more narrower than the monochromator's slit (2 mm), it is completely illuminated along its axis in the slit function configuration while only a part of it (2 mm out of 3 mm) is illuminated during the pixel function scan. The OGSE optical bench, over which are mounted the aforementioned electro-optical elements, is fixed above an Hexapod mount (Symetrie model BREVA). Thanks to the 6 degrees of freedom of the hexapod it is possible to translate and rotate the collimated test beam within the MAJIS field of view. In this way the image of the test slit can be acquired on different pixels across the instrument's field of view. The spatial characterization has been performed on three test positions placed on the MAJIS boresight and on the two extremes of the FOV. The hexapod positioning performances are calibrated with respect to the pivot point placed on the collimator's pupil. With respect to the pivot point, located at position X_P =+364 mm, Y_P =-54.6 mm and Z_P =+266 mm from the center of the mobile platform, the hexapod performances make it possible to reach the displacements, resolutions, repeatabilities and accuracies reported in Table I.

Hexapod DOF	Displacement axis by axis	Resolution	Repeatability	Accuracy
T_X	$\pm$50 mm	2 μm	$\pm$4 μm	$\pm$50 μm
T_Y	$\pm$50 mm	2 μm	$\pm$4 μm	$\pm$50 μm
T_Z	$\pm$20 mm	2 μm	$\pm$4 μm	$\pm$50 μm
R_X	$\pm 7^\circ$	1 arcsec	$\pm$5 arcsec	$\pm$50 arcsec
R_Y	$\pm 7^\circ$	1 arcsec	$\pm$5 arcsec	$\pm$50 arcsec
R_Z	$\pm 6^\circ$	1 arcsec	$\pm$5 arcsec	$\pm$50 arcsec

TABLE I. Hexapod BREVA - positioning performances specification for pivot point. Displacements are relative to the single axis with the other ones positioned at half of their stroke. Repeatability is given accordingly to ISO 230-2: unidirectional repeatability is given within ± 2 standard deviations.

The OGSE is placed in front of the Thermovacuum Chamber (TC) in which the MAJIS Optical Head (OH) is kept under vacuum and at cryogenic operative temperatures by means of a dedicated thermal control system. The optical beam of the collimator reaches the MAJIS' entrance pupil by means of a window (made in CaF_2 glass to guarantee high transmission across the 0.5-5.5 μm spectral range) placed on the chamber's door. During the measurements the MAJIS scan mirror is kept fixed on the boresight position.

During measurements, both MAJIS and the OGSE, are controlled by the Electrical Ground Support Equipment (EGSE), which

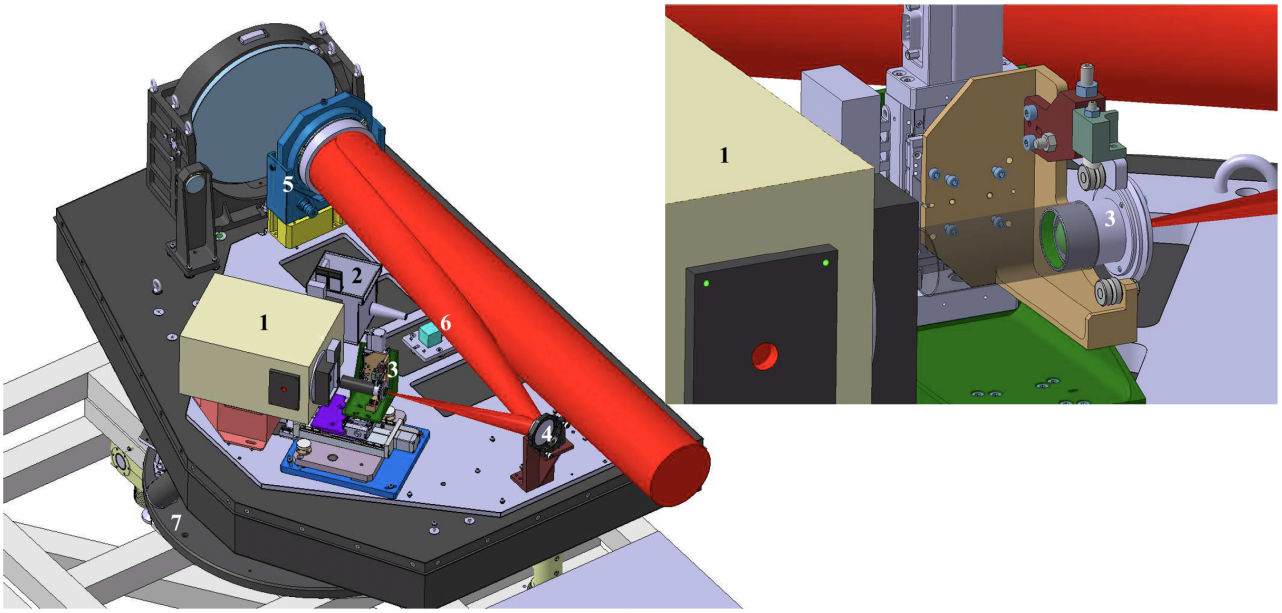

FIG. 2. Configuration of the OGSE setup realized in Leonardo Company for the characterization of the MAJIS OH: 1. Monochromator, 2. Monochromator's source, 3. Test slit, mounted on a rotating and translating X-Y stage, 4. Collimator's secondary mirror, 5. Collimator's off-axis parabola, 6. Reference cube mirror, 7. Hexapod mount. The collimated optical beam is rendered in red. Image courtesy: Leonardo.

manages the configuration, and the data acquisitions. In particular, during the spatial scans, the EGSE controls the positioning of the test slit through the 2 axes motorized Micronix linear stages, and commands the MAJIS acquisitions once it reaches the planned configuration. In this way all MAJIS measurements are synchronous because are performed on programmed and controlled configurations of the optical setup. The telemetry of the OGSE configuration (positions of the hexapod and linear stage, monochromator, sources voltages, and currents, etc.) are stored synchronously with the MAJIS acquisitions so as to correlate science and OGSE telemetry data. Finally, for each scan MAJIS acquires dark current (closing the internal shutter) and background data (switching off the light sources in the monochromator) necessary to remove the detector's and ambient noises. This operation is performed during the post-processing of the data.

2. *Calibration setup in IAS*

A calibration device to characterize the radiometric, spectral and spatial performances of MAJIS has been developed at the Institut d'Astrophysique Spatiale (hereafter IAS). This device and the details of the measurement campaigns are presented in a companion paper [16]. In the following, we briefly describe the setups and the measurements from which the spatial characterization was inferred and checked. The main setup dedicated to the spatial measurements is the so-called "Optical Path 1" (OP1) that provides a beam corresponding to a collimated source with a small spatial extent. OP1 was mainly composed of the following elements: (1) a light source, which can be selected as a QTH lamp or a blackbody in order to provide a flux covering the entire spectral range of the instrument, the QTH lamp is mainly used for the VISNIR channel and the blackbody for the IR channel; (2) a monochromator set at zero-order; and (3) a series of mirrors which projects the monochromator zero-order output to infinity resulting in a beam wide enough to cover the entire MAJIS input baffle. The monochromator output was a rectangular slit of adjustable width. An additional and adjustable circular aperture was also placed right after this slit. The source imaged by MAJIS could thus have several spatial dimensions, from a rectangle of about 20 nominal pixels long to a few pixels wide, or a disk ranging from one to a few pixels in diameter. The intensity profile of the source disk is much closer to a Gaussian function than to a gate function due to diffraction. OP1's optical elements were located in an opaque optical bench, flushed with nitrogen, and the beam was illuminating the vacuum chamber through the window, in which MAJIS was installed on a mobile hexapod. With this OP1 source, scans with steps of 1/5 IFOV were performed along-slit and across-slit (fixed source, rotating MAJIS).

Other optical paths of the IAS calibration device were also used to produce data useful for checking the spatial performances, especially the size of the FOV: they refer to "OP3, OP4 and OP5" setups [16]. OP3 and OP4 provided a collimated source illuminating the entire FOV of the 2 channels to assess the radiometric performances of the instrument[10]. These setups were also of special interest for retrieving the size of the FOV, the co-registration between the two MAJIS channels and an estimate of

the spatial response at the edges of the FOV. Both OPs consist of an integrating sphere connected to a light source (QTH lamp or black body emitter) to produce a flat field large enough to cover the full FoV of MAJIS. The main difference is that OP4 was located in the thermal chamber, avoiding absorption from the entry window and removing a parasitic thermal background [16]. Finally, OP5 enabled the acquisition of images in reflectance of a calibration synthetic target with a well-defined edge and of natural rock samples to assess performance in terms of pixel function. These data and their analyses are presented in a companion paper [13].

C. Measurements cases

1. LDO

The spatial scans are performed on three positions of the FOV, corresponding to boresight (0°) and near the left edge (-1.7°) and right edge (1.7°) of the FOV. In this way, it is possible to verify the variation of the spatial performances across the FOV. These measurements are made with the MAJIS OH stabilized at average operative temperature T_{op-avg}=130 K. Possible changes in the spatial response due to thermal stress were investigated by performing the on-axis slit function measurement at the minimum and maximum expected temperatures corresponding to the operative cold ($T_{op-cold}$=110 K) and hot (T_{op-hot}=150 K) cases. Table II reports the integration times for the VISNIR and IR channels for each spatial scan.

Function	FOV Position	Nom T_{op}		Min T_{op}		Max Avg T_{op}	
		t_{int} (ms)		t_{int} (ms)		t_{int} (ms)	
		VISNIR	IR	VISNIR	IR	VISNIR	IR
Pixel	-1.7°	40	11	N.A.	N.A.	N.A.	N.A.
	0°	11	11	N.A.	N.A.	N.A.	N.A.
	1.7°	20	11	N.A.	N.A.	N.A.	N.A.
Slit	-1.7°	20	28	N.A.	N.A.	N.A.	N.A.
	0°	15	20	50	22	50	22
	1.7°	40	28	N.A.	N.A.	N.A.	N.A.

TABLE II. Summary of the measurements performed in LND to derive MAJIS pixel and slit functions measured on three position of the FOV and for three different temperature set points corresponding to the nominal, minimum and maximum cases.

2. IAS

a. Monochromator scan As for LDO measurement, the spatial scans are performed on three positions of the FoV, corresponding to boresight (0°) and two offset field positions (-1.5°, corresponding to the negative field, and 1.5°, corresponding to the positive field, in the "left" and "right" part of the FOV, respectively, according to the nomenclature used in a companion paper[10]). Spatial measurements were acquired for two MAJIS thermal configurations: optical head at 126 K and detector at 88 K (nominal case, extended measurements), and optical head at 137 K and detector at 96 K (hot case, complementary measurements). In Table III we report the integration times of the measurements performed at IAS to characterize the Pixel Function. The size of the OP1 spot on the MAJIS detector was estimated to be around 40 μm (reps. 70 μm) on the VISNIR (resp. IR) channel. After the calibration campaign, we noticed the OP1 monochromator flux provided a zero-order spectral profile that was not constant from step to step. A high-frequency (sinusoid-like on the IR channel) perturbation could be seen propagating along the spectrum of the illuminating source. This perturbation had a period of about 50 (28) physical pixels for the VISNIR (IR) channel. To mitigate this effect, median filtering across 2 (4) periods was applied to the IAS VISNIR (IR) scan data prior to retrieving the pixel response from a Gaussian fitting procedure. The measurements dedicated to the slit function were, however, not exploitable because of this input signal artifact.

Function	FOV Position	OH at T=126 K		OH at T=137 K	
		t_{int} (ms)		t_{int} (ms)	
		VISNIR	IR	VISNIR	IR
Pixel	-1.5°	400	60	N.A.	N.A.
	0°	N.A.	60	400	60
	1.5°	400	60	N.A.	N.A.

TABLE III. Summary of the measurements performed in IAS to derive MAJIS pixel function measured on three position of the FOV and for two different Optical Head temperature set points.

b. Full FOV acquisitions Acquisitions for which the entire FoV was illuminated by a flat-field signal were used for determining the FOV size and the position of the two channels on the detectors and for deriving the pixel function response using a knife edge test at the edges of the FoV (at -1.7°, corresponding to the negative edge or "left" position of the detector, and 1.7°, corresponding to the positive edge or "right" position of the detector according to the nomenclature used in a companion paper[10]). As presented in section II B 2, OP3- and OP4-based images provided such data for both channels. The images were acquired using various integration times according to the objectives of the radiometric calibration, and we selected the most favorable frames to extract the spatial parameters.

III. GROUND MEASUREMENTS AND RESULTS

A. Pixel Function

During the Pixel Function scans, the test slit is translated perpendicularly to the MAJIS slit (Fig. 1). Each scan performed at LDO (resp. IAS) consists of 31 (resp. 41) steps. Each LDO scan consists of 31 steps. At each step, the test slit is shifted at increments of 46 μm/step by the OGSE, corresponding to a shift of 7.2 μ on the MAJIS focal plan. In total, the scan spans across ≈6 (8 for IAS resp.) nominal pixels or ≈12 (resp. 16) physical pixels.

The data collected with the LND setup allow us to derive the Pixel Function profiles as shown in Fig. 3 for 2 adjacent physical pixels (sample$_{1,2}$, 18 μm pixel) selected on the on-axis position. For each scan are shown the best gaussian fit profiles. The fitted FWHM measured on the two samples under investigation and their separation measured as the difference between the centers of the two gaussian fit curves are reported in Tables IV-V for the VISNIR and IR channels, respectively. Apart frommeasuring the pixel response FWHM, this method allows to derive the effective separation between the two pixels as given by the distance between the centers of the two gaussians.

Examples of the resulting Pixel Function profiles are shown in Fig. 4 for a set of samples selected on the on-axis positions at IAS premises.

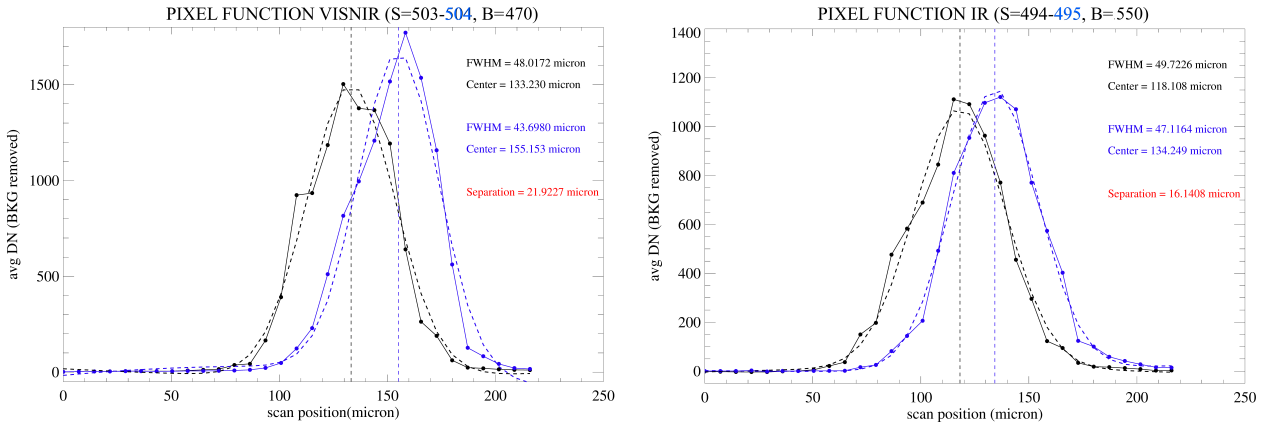

FIG. 3. MAJIS pixel functions measured profiles (solid lines) and fitted curves (dashed lines) on the on-axis position as measured with the LND setup at physical pixel resolution. Left panel: VISNIR pixel function measured at sample=503 (black) and 504 (blue) at band=470 (1347 nm). Right panel: IR pixel function measured at sample=494 (black) and 495 (blue) at band=550 (3988 nm).

The fitted FWHM measured on the two samples under investigation (sample$_{1,2}$, physical pixels of 18 μm) is averaged and reported in Tables IV – V from LDO measurements, for the VISNIR and IR channels, respectively, and for three positions of the field of view. Similarly, the analysis of the scans from IAS measurements are reported on Tables VI – VII. For the sake of brevity, rather than reporting all scans and fit figures, we summarize the relevant results in the aforementioned Tables.

The signal at both edges of the slit can be modeled when the FOV is fully illuminated, providing an alternative approach to evaluate the pixel function assuming that the shape is mainly due to diffraction. The knife edge signal modeling is performed by fitting a Gaussian instrument transfer function response convoluted to a Heaviside step function. The center of the simulated pixels on the resulting convolution is shifted to match the center of the pixels observed on MAJIS acquisitions. This approach is quite successful at modeling the evolution of the signal at both edges of the slit as shown in Fig. 5. The knife edge tests from IAS measurement are reported in Table VI-VII.

Both datasets clearly show a progressive deterioration of the VISNIR pixel function's FWHM$_P$ at both wavelengths (750 nm and 1500 nm) when moving from the negative to the positive field. In fact, the best performances are reached on the negative field where FWHM $\leq$ 30 μm on the LDO dataset while it increases up to 130 μm for on the positive field. This effect could be

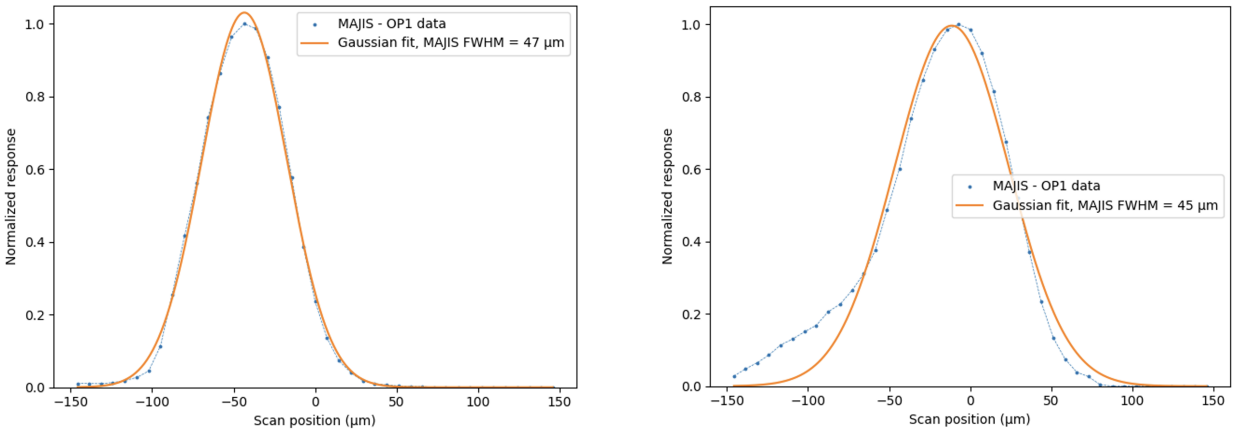

FIG. 4. MAJIS pixel functions measured profiles (blue solid lines) and fitted curves (orange lines) on the on-axis position as measured with the IAS setup. Left panel: VISNIR pixel function measured at sample=491 at band=550. Right panel: IR pixel function measured at sample=486 at band=150.

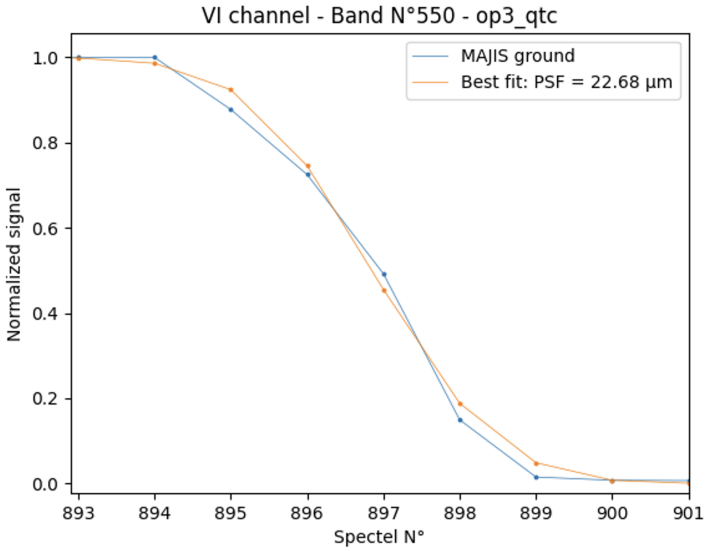

FIG. 5. Examples of an IAS OP3 observation knife edge fitting for the band=550 of the VISNIR channel on the left edge of the FOV. The resulting FWHM of the pixel function is indicated.

FOV Position	$Sample_1$	$Sample_2$	Band	$Center_1$ (μm)	$Center_2$ (μm)	$FWHM_{18\mu m}$ (μm)	$FWHM_{36\mu m}$ (μm)
-1.5°	133	134	870	105.87±0.13	126.17±0.23	24.31±0.20	26.74±0.22
-1.5°	133	134	470	111.43±0.06	130.76±0.29	23.98±0.20	26.38±0.22
0°	503	504	870	129.62±0.73	153.13±0.82	45.94±0.99	50.53±1.10
0°	503	504	470	133.23±0.72	155.15±0.76	45.86±0.93	50.45±1.02
1.5°	867	868	870	84.33±0.92	100.71±1.14	96.40±1.97	106.04±2.17
1.5°	867	868	470	80.37±1.23	93.62±1.43	81.11±2.94	89.22±3.23

TABLE IV. MAJIS-VISNIR channel pixel function measured on three positions of the FOV and at two spectral bands 470 (corresponding to wavelength 1347 nm) and 870 (2083 nm) in LDO. The average FWHM measured on two physical (18 μm) contiguous pixels and on the nominal 36 μm pixel are reported. The wavelengths values associated to the bands are given by the spectral calibration discussed in a companion paper [8].

explained by a residual misregistration of the detector plane, which has not been fully compensated during the alignment phase

FOV Position	$Sample_1$	$Sample_2$	Band	$Center_1$ (μm)	$Center_2$ (μm)	$FWHM_{18\mu m}$ (μm)	$FWHM_{36\mu m}$ (μm)
-1.5°	125	126	150	110.57±0.25	128.72±0.47	24.18±0.41	26.60±0.45
-1.5°	125	126	550	128.92±0.55	148.79±0.27	25.34±0.46	27.87±0.51
0°	494	495	150	105.87±0.88	122.60±0.54	44.45±0.99	48.89±1.10
0°	494	495	550	118.11±0.59	134.25±0.38	48.41±0.68	53.25±0.75
1.5°	864	865	150	132.50±0.59	150.77±0.53	33.13±0.66	36.44±0.73
1.5°	864	865	550	144.67±0.69	162.67±0.70	37.32±0.82	41.05±0.90

TABLE V. Same as Table IV but for MAJIS-IR channel at bands 150 (corresponding to wavelength 2713 nm) and 550 (3988 nm).

Data OP	FOV position	$Sample_1$	$Sample_2$	Band	$FWHM_{18\mu m}$ (μm)	$FWHM_{36\mu m}$ (μm)
OP3	-1.7°			150	44.2	49.82
OP3	-1.7°			550	36.3	43.56
OP3	-1.7°			700	51.7	56.38
OP1	-1.7°	138	139	550	43.3	49.1
OP1	-1.5°	138	139	700	41.52	47.66
OP1	0°	493	494	150	68.90	72.22
OP1	0°	493	494	550	47.17	52.34
OP1	0°	493	494	700	47.85	52.99
OP1	1.5°	850	851	700	102.27	104.4
OP3	1.7°			150	110.7	112.75
OP3	1.7°			550	52.3	56.88
OP3	1.7°			700	56.9	61.06

TABLE VI. Same as Table IV (VISNIR channel) but from IAS measurements at bands 150 (corresponding to wavelength 754 nm), 550 (1496 nm) and 700 (1770 nm). For the measurements at the edge of the FOV (±1.7°), the reported FHWM corresponds to the average values over several wavelengths.

Data OP	FoV position	$Sample_1$	$Sample_2$	Band	$FWHM_{18\mu m}$ (μm)	$FWHM_{36\mu m}$ (μm)
OP4	-1.7°			150	30.3	39.53
OP4	-1.7°			550	32.1	40.68
OP4	-1.7°			700	35.9	43.27
OP1	0°	486	487	150	47.54	52.7
OP1	0°	486	487	450	49.20	54.07
OP1	1.5°	843	844	150	30.34	39.53
OP1	1.5°	843	844	450	46.14	51.48
OP4	1.7°			150	21.9	36.22
OP4	1.7°			550	27.7	38.16
OP4	1.7°			700	31.6	40.32

TABLE VII. Same as Table V (IR channel) but from IAS measurements at bands 150 (corresponding to wavelength 2713 nm), 550 (3988 nm) and 700 nm (4480 nm).

due to the program's schedule constraints. When comparing these results with the scientific requirement (spatial FWHM $\leq$ 54 μm), we see that the pixel function response is within the requirement on both negative and on-axis positions while it is out of the requirement by a factor ≈2 on the positive field. The same approach adopted for the VISNIR channel has been applied to derive the pixel function parameters for the IR channel. In general, the signal on the profiles at band=150 is much lower than the one on the b=550 profile resulting in worse fits. A similar trend is observed in the IAS measurements at band 150 vs. 450 (Table VII). Differently from the VISNIR channel, the IR response is characterized by a better $FWHM_P$ across the entire field of view at both spectral bands showing a measured FWHM better than the scientific requirement (54 μm) in most cases.

B. Slit Function

During the Slit Function scans performed in LDO the test slit is placed parallel to MAJIS slit direction (Fig. 1). Also in this case each scan spans across 31 steps. On each step the test slit position is shifted at increments of 46 μm/step by the OGSE corresponding to a shift of 7.2 μm on the MAJIS focal plane. This value corresponds to $0.2 \cdot px_{nom}$ where px_{nom}=36 μm is the nominal pixel obtained by binning two physical pixels of 18 μm each. In total the scan spans across ≈6 nominal pixels or

≈12 physical pixels. Analyzing the evolution of the signal measured by a given pixel during the scan, we observe a null signal when the position of the test slit falls well outside the pixel's position followed by a fast increase when the two positions are intercepting each other. The signal reaches a maximum when the test slit's position is aligned with respect to the pixel center and immediately after it decreases again. The overall shape of the profile is simil-gaussian, with deviations caused by the not perfectly symmetrical response of the OGSE and of the instrument.

Examples of Slit Function profiles measured on the on-axis position are shown in Fig. 6 for a given pixel for both VISNIR and IR channels. For each spatial scan are shown the best gaussian fit profiles. For sake of conciseness we do not include the figures for each single scan but only the results of the fits in Table VIII for the VISNIR channel and in Table IX for the IR.

FoV Position	Sample	Band	Center (μm)	FWHM$_{18\mu m}$ (μm)	FWHM$_{36\mu m}$ (μm)
-1.5°	146	870	94.16±0.26	43.33±0.35	47.67±0.38
-1.5°	146	470	93.52±0.26	42.87±0.35	47.16±0.38
0°	504	870	111.05±0.81	54.87±1.36	60.36±1.50
0°	504	470	109.16±0.99	57.18±1.73	62.90±1.90
1.5°	872	870	93.65±0.25	43.99±0.33	48.39±0.36
1.5°	872	470	92.95±0.26	43.75±0.35	48.12±0.38

TABLE VIII. MAJIS-VISNIR channel slit function measured in LDO on three positions of the FOV and at two spectral bands 870 (corresponding to wavelength 2083 nm) and 470 (1347 nm). The wavelength values associated with the bands are given by the spectral calibration discussed in a companion paper[8].

FoV Position	Sample	Band	Center (μm)	FWHM$_{18\mu m}$ (μm)	FWHM$_{36\mu m}$ (μm)
-1.5°	118	80	80.06±0.60	61.78±0.90	67.96±0.99
-1.5°	118	550	84.65±0.78	68.74±1.36	75.61±1.50
0°	485	80	92.67±0.80	44.49±1.09	48.94±1.20
0°	485	550	84.37±0.69	63.81±1.06	70.19±1.17
1.5°	854	80	109.59±0.68	39.11±0.90	43.02±0.99
1.5°	854	550	105.65±0.63	46.58±0.91	51.24±1.00

TABLE IX. Same as Table VIII but for the MAJIS-IR channel at spectral bands 80 (corresponding to wavelength 2500 nm) and 550 (3988 nm).

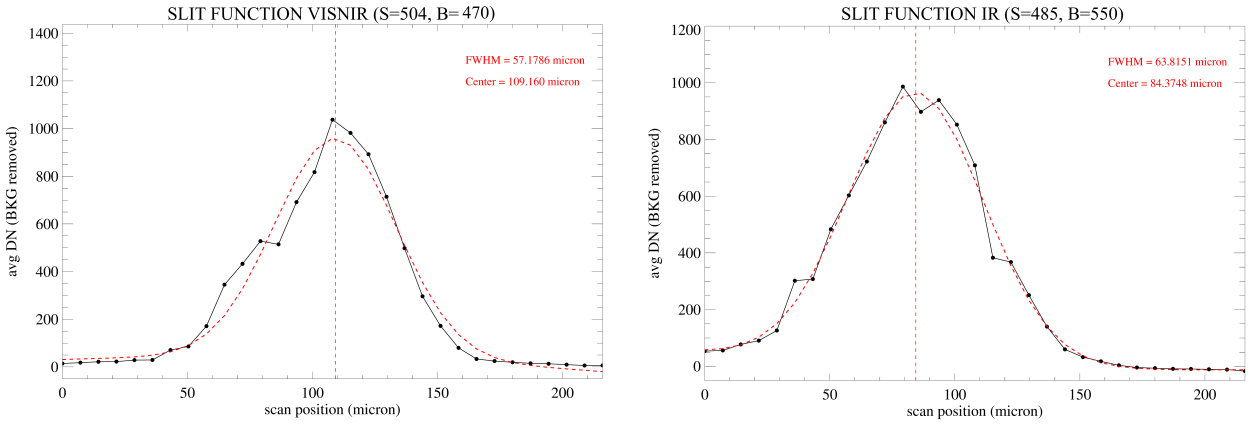

FIG. 6. Examples of MAJIS slit function measured (black points) and fitted (red lines) profiles on the on-axis position with the LDO setup. Left panel: VISNIR slit function measured at sample=504 and band=470 (1347 nm). Right panel: IR slit function measured at sample=485 and band=550 (3988 nm).

For the VISNIR channel, the measured values of the slit function FWHM are in general within the requirement (spatial FWHM ≤ 54 μm), with only a very small deviation on the on-axis position. For the IR channel, we measure FWHM values higher by at most 10 μm than the requirement (spatial FWHM ≤ 54 μm) on three out of six cases, e.g. on the on-axis position at b=550 and on both bands on the negative field.

C. VISNIR and IR channels alignment during the on-ground calibration

The two 1024×1024 Teledyne detectors are illuminated by the instrument's FoV across 800 consecutive rows of 18 μm pixels, while the dispersion of wavelengths occurs over 1016 columns of 18 μm spectels. The focal plane electronics have the capability of reading out only part of the 1024 rows corresponding to the exact size of the image. This window is defined by the start row and the number of rows (maximum value: 1024 – start row value). The knowledge of the FoV start row (row value corresponding to the edge of the nominal FoV) is critical for the nominal operation of the MAJIS instrument. For the vast majority of in-flight acquisitions, 400 nominal pixels corresponding to 800 rows will be transmitted so as to cover the full FOV, removing rows with no signal. The position and the size of the instrument's FoV were measured using various sources during the calibration campaign. They can be monitored in-flight thanks to acquisitions with the ICU (Internal Calibration Unit, see Section VII).

The start row is defined as the physical pixel for which the signal level reaches half of the stabilized signal (Fig. 7).

The results of the nominal FoV positions (start row, end row) for both channels are shown in Table XVII. The sizes of the nominal FoV for both channels are in line with the expected nominal size (800 rows). For the VISNIR channel (resp. the IR channel), the rows selected based on these ground measurements are 96-895 (resp. 90-889). The start row is thus not the same for both channels due to a mis-registration between them. This offset between the two channels along the slit direction is compensated by telecommand since the start row can be different for the VISNIR and IR channels thanks to one dedicated parameter for each channel. It should be noted that the VISNIR FoV has a small rotation along wavelength (see Section VI).

VISNIR band (source)	Bottom (px number)	Top (px number)	IR band (source)	Bottom (px number)	Top (px number)
150	95.68	895.60	150	90.66	891.00
550	95.83	898.15	550	89.72	890.50
700	96.86	897.38	700	89.20	890.33

TABLE X. Position of the start and end rows of the FoV for both channels from OP3 and OP4 data.

IV. ENSQUARED ENERGY DERIVATION

Taking advantage of the repeatability of the measurements on the same pixels during the VISNIR spatial scans it is possible to derive the Ensquared Energy Distribution (EED) for the on-axis position at bands 150 and 550. The EED allows for measuring the fraction of the flux effectively measured by one pixel with respect to the flux in input. The EEDs shown in Fig. 8-9 are built from the interpolation of the pixel (along the vertical axis) and slit functions (along the horizontal axis). The white square corresponds to the nominal pixel (36 × 36 μm) over which it is integrated the relative flux.

A similar analysis cannot be repeated for the IR channel because we do not have enough measurements taken during the pixel and slit function scans on a suitable set of paired pixels.

V. VARIABILITY OF THE SPATIAL RESPONSES AS A FUNCTION OF THE INSTRUMENT OPERATIVE TEMPERATURE

A. Slit function

Since the MAJIS instrument is operating at cryogenic temperatures by mean of a passive thermal design [12], its equilibrium temperature depends on the thermal environment occurring on the interfaces with the spacecraft bus and from the orientation of the passive radiators with respect to nearby objects. One radiator is coupled to the OH structure (including the VISNIR detector), and a second one with the IR detector. The nominal, minimum and maximum range of expected temperatures are computed through an engineering thermal model and reflect different orbital scenarios of the mission (see details in [12]). For this reason it is important to verify any possible deviation of the instrument response measured in the nominal thermal case when the OH temperature reaches the minimum or the maximum expected temperature because some scientific observations will occur in such conditions. Table XI-XII detail the results of the measurements of the slit functions performed on two physical pixels at the minimum and maximum operative temperatures for the VISNIR and IR channels, respectively, using the LND setup. The corresponding pixel function measurements were not performed due to the compressed schedule of the calibration campaign.

The measurements show different trends of the instrument response as a function of the temperature: on the VISNIR channel we observe an improvement of the slit function at the maximum temperature where the FWHM becomes smaller by a few microns. At the minimum temperature, instead, a marginal worsening occurs. On the IR channel we observe in general a broadening of the slit function FWHM with respect to the nominal case at the maximum temperature while for the minimum

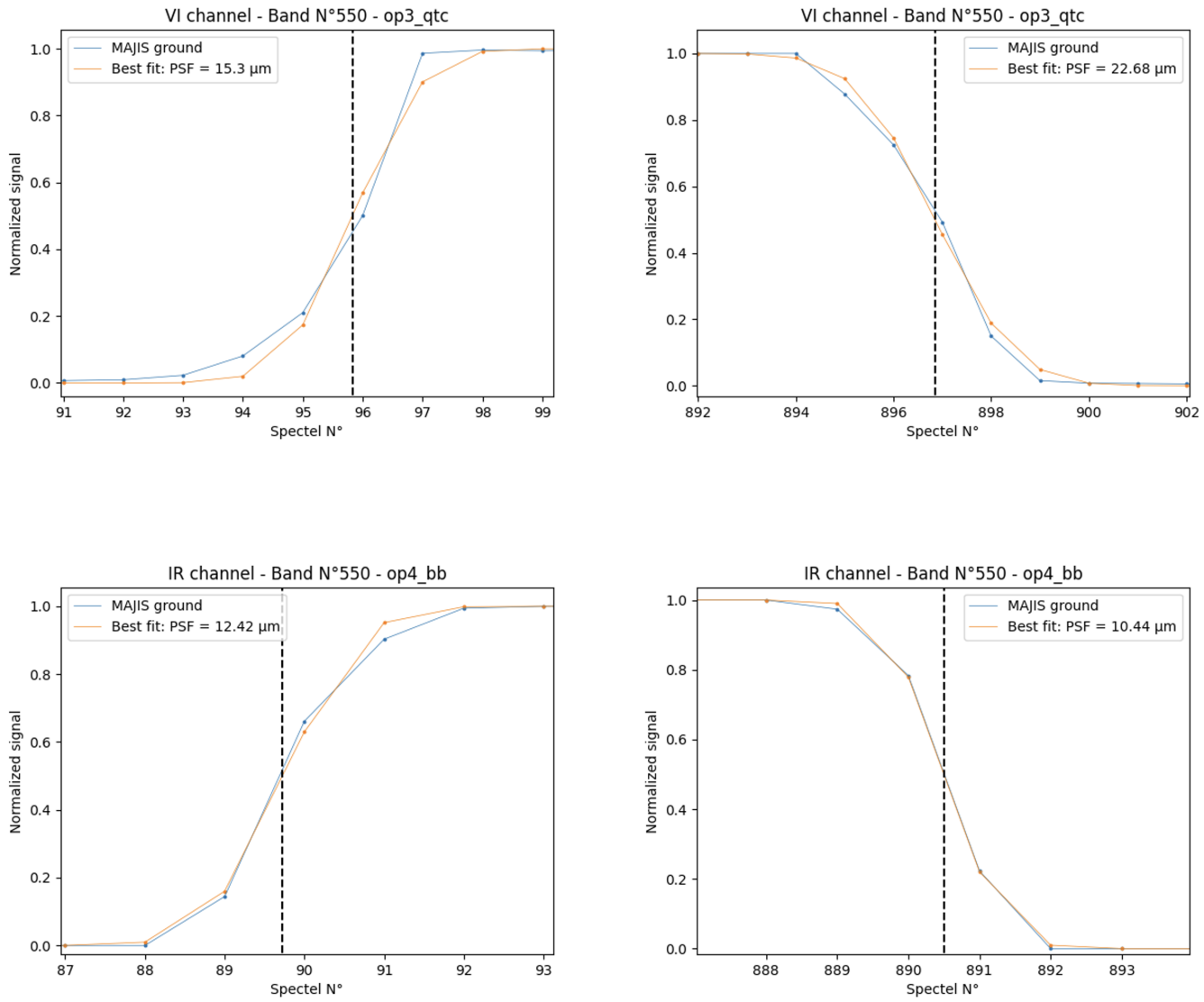

FIG. 7. Model fit with the spatial profile of the signal measured at FoV position -1.7° (left edge of the FOV, left panel) and at 1.7° (right edge of the FOV, right panel) for band 550 on the VISNIR channel (top panels) and on the IR channel (bottom panels). The blue points correspond to the profiles observed during ground calibration with OP3 and OP4 IAS setups and the orange points correspond to the best fit points. The vertical dashed lines indicate the retrieved FOV edges.

T_{op} (K)	Sample	Band	FWHM$_{18\mu m}$ (μm)	FWHM$_{36\mu m}$ (μm)	ΔFWHM$_{36\mu m}$ (μm)
min	504	870	58.12±1.42	63.93±1.56	3.57±3.06
min	504	470	58.16±1.40	63.98±1.54	1.08±3.44
nom	504	870	54.87±1.36	60.36±1.50	==
nom	504	470	57.18±1.73	62.90±1.90	==
max	504	870	51.35±1.33	56.48±1.46	-3.88±2.96
max	504	470	51.83±1.39	57.01±1.53	-5.89±3.43

TABLE XI. MAJIS-VISNIR channel slit function measured on-axis at two spectral bands 870 (corresponding to wavelength 2083 nm) and 470 (1347 nm) as a function of the operative temperature of the OH. The ΔFWHM corresponds to the difference of the FWHM$_{36\mu m}$ at min and max temperature cases with respect to the nominal one.

temperature case the two pixels show an opposite behavior on the two bands. Finally, it is interesting to note in Tables XI-XII how the spatial performances of the VISNIR channel are in general better and less sensitive to instrument's temperature changes than the ones measured on the IR.

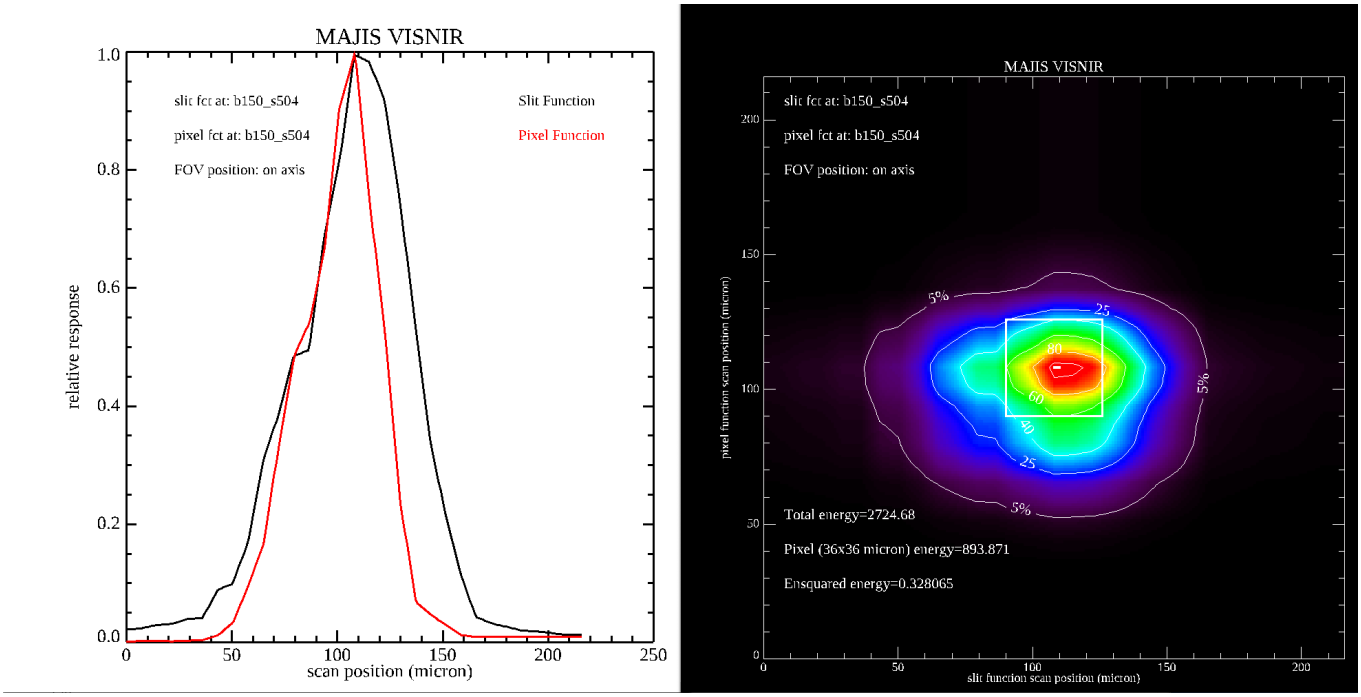

FIG. 8. Ensquared Energy Distribution computed for the VISNIR channel at b=150 and physical sample=504 (on axis position). Left panel: normalized slit and pixel functions as a function of spatial scan. Right panel: EED derived from the normalized slit and pixel functions. The colors run from white (=1) to green (=0.5) to black (=0). The total energy value corresponds to the integral computed on the entire distribution while the nominal pixel energy refers to the integral limited to the 36×36 μm (white square) area. The ensquared energy value (32.8%) is the ratio between the total energy and the energy effectively measured by the pixel.

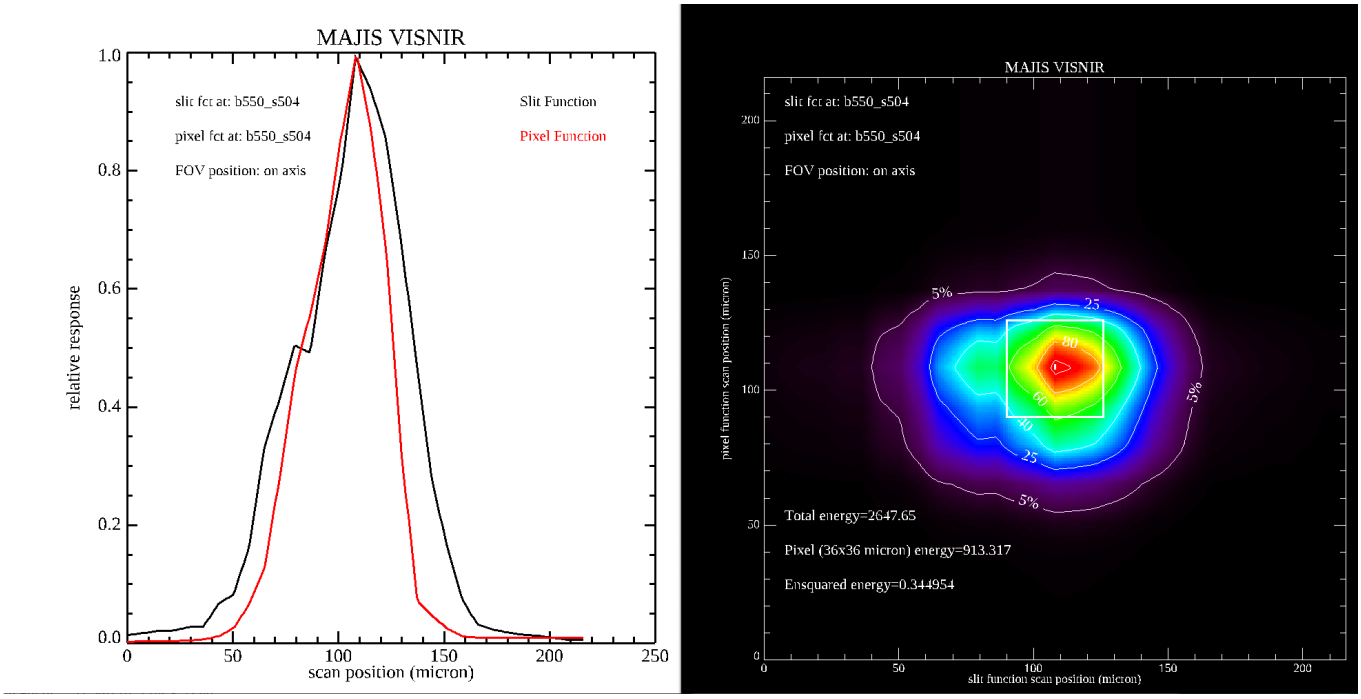

FIG. 9. The same as Fig. 8 but at b=550 and physical sample=504 (on axis position). In this case the ensquared energy value is 34.5%.

T_{op} (K)	Sample	Band	FWHM$_{18\mu m}$ (μm)	FWHM$_{36\mu m}$ (μm)	ΔFWHM$_{36\mu m}$ (μm)
min	532	80	62.35±1.05	68.58±1.15	19.64±2.35
min	532	550	56.32±0.95	61.95±1.04	-8.24±2.21
nom	485	80	44.49±1.09	48.94±1.20	==
nom	485	550	63.81±1.06	70.19±1.17	==
max	540	80	54.28±0.92	59.71±1.01	10.77±2.21
max	540	550	66.74±1.12	73.41±1.23	3.22±2.40

TABLE XII. MAJIS-IR channel slit function measured on-axis at two spectral bands 80 (corresponding to wavelength 2500 nm) and 550 (3988 nm) as a function of the operative temperature of the OH. The ΔFWHM corresponds to the difference of the FWHM at min and max temperature cases with respect to the nominal case.

B. Pixel function

The MAJIS optical design was developed to maintain similar performances under different operative temperatures. However, the exploration of the thermal effect was very limited because of the schedule constraints. The pixel spatial response of the IR channel has been explored from the IAS dataset at two different temperatures (Table XIII). Based on the limited set of measurements, no variation is observed.

T_{OH} (K)	Sample$_1$ (μm)	Sample$_2$ (μm)	Band	FWHM$_{18\mu m}$ (μm)	FWHM$_{36\mu m}$ (μm)
126	486	487	150	47.52	52.30
126	486	487	450	49.20	54.12
137	486	487	150	34.06	37.47
137	486	487	450	60.98	67.08

TABLE XIII. Comparison of the pixel function for the IR channel at two wavelengths and at two different temperatures.

VI. MEASUREMENT OF THE KEYSTONE DISTORTION

Keystone is an optical distortion affecting the response of grating spectrometers [17] introducing a pixel to pixel magnification which changes with the wavelength. The net effect is a spectral tilt of the spectrum along the focal plane. The MAJIS optical design includes corrective elements along the optical path of the spectrometers able to compensate for the keystone aberration to a degree below 1 nominal pixel across the full spectral range and field of view. Moreover, the instrument's opto-mechanical design has been realized with the aim of guaranteeing a high level of alignment among the spectrometer's slit direction, the grooves' direction of the two gratings, and detectors' sides. Thanks to the adopted calibration approach, the spatial scans used for the pixel function (Table IV-V) are suitable to measure the keystone effect by calculating the difference between the centers of a given pixel sample position (for example, for the VISNIR 133 or 134 for the negative field case; 503 or 504 for the on axis position; 867 or 868 for the positive field) between the two spectral bands (b_1=150, b_2=550). As an example, on sample 503 we measure a difference between centers' positions equal to Δ=Center$_1$(b=150)-Center$_1$(b=550)=(129.62$\pm$0.73)-(133.23$\pm$0.72)=-3.51$\pm$1.45 μm corresponding to a keystone angle of:

$$tg(\alpha_{Key}) = \frac{\Delta}{d_{px} \cdot (b_2 - b_1)} \tag{4}$$

or an α_{Key} = -2.79$\cdot$ 10^{-2} deg. The resulting keystone, or maximum displacement between the two extreme spectral bands on the detector, is equal to Δ_{Key}=tg(α_{Key})$\cdot$(18 μm $\cdot$ 1024) = -8.99 μm. A similar calculation applied on the whole dataset gives the results shown in Tables XIV-XV.

FOV Position	Sample	Δ (μm)	α_{Key} (deg)	Δ_{Key} (μm)
-1.5°	133	$-5.56^{-5.37}_{-5.75}$	$-4.42^{-4.27}_{-4.57}\cdot 10^{-2}$	$-14.23^{-13.74}_{-14.72}$
-1.5°	134	$-4.59^{-4.07}_{-5.11}$	$-3.65^{-3.24}_{-4.07}\cdot 10^{-2}$	$-11.75^{-10.42}_{-13.08}$
0°	503	$-3.61^{-2.16}_{-5.06}$	$-2.87^{-1.72}_{-4.02}\cdot 10^{-2}$	$-9.24^{-5.53}_{-12.95}$
0°	504	$-2.02^{-0.44}_{-3.66}$	$-1.61^{-0.35}_{-2.86}\cdot 10^{-2}$	$-5.17^{-1.13}_{-9.22}$
1.5°	867	$3.96^{6.11}_{1.81}$	$3.15^{4.86}_{-1.44}\cdot 10^{-2}$	$10.13^{15.64}_{4.63}$
1.5°	868	$7.09^{9.66}_{4.52}$	$5.64^{7.69}_{3.60}\cdot 10^{-2}$	$18.15^{24.72}_{11.57}$

TABLE XIV. Keystone distortion on MAJIS VISNIR optical channel.

FOV Position	Sample	Δ (μm)	α_{Key} (deg)	Δ_{Key} (μm)
-1.5°	125	$-18.35^{-17.55}_{-19.15}$	$-0.15^{-0.14}_{-0.15}$	$-46.98^{-44.93}_{-49.02}$
-1.5°	126	$-20.07^{-19.33}_{-20.81}$	$-0.16^{-0.15}_{-0.17}$	$-51.38^{-49.48}_{-53.27}$
0°	494	$-12.24^{-10.77}_{-13.71}$	$-9.74^{-8.57}_{-10.90}\cdot 10^{-2}$	$-31.33^{-27.57}_{-35.09}$
0°	495	$-11.65^{-10.73}_{-12.57}$	$-9.27^{-8.54}_{-10.00}\cdot 10^{-2}$	$-29.82^{-27.47}_{-32.18}$
1.5°	864	$-12.17^{-10.89}_{-13.45}$	$-9.68^{-8.67}_{-10.70}\cdot 10^{-2}$	$-31.15^{-27.88}_{-34.43}$
1.5°	865	$-11.90^{-10.67}_{-13.13}$	$-9.47^{-8.49}_{-10.44}\cdot 10^{-2}$	$-30.46^{-27.31}_{-33.61}$

TABLE XV. Keystone distortion on MAJIS IR optical channel.

The VISNIR channel keystone distortion results shown in Table XIV evidence a negative angle trend from the axis towards the negative field and a positive angle on the positive field. Overall the effect is very small and well-within the scientific requirement of $\Delta_{Key} < 36$ μm. On the contrary, for the IR channel (Table XV) the keystone is similar to the requirement for the on-axis and on the positive field but reaches values larger by $\approx$11-15 μm than the requirement on the negative field pixels. The analysis of the smile distortion, e.g. the curvature of the slit image on the detector, is described in a complementary paper [8].

		ICU ground data		ICU flight data	
FOV position	Band	FWHM VISNIR (μm)	FWHM IR (μm)	FWHM VISNIR (μm)	FWHM IR (μm)
-1.7°	150	39.80	35.09	37.68	37.44
-1.7°	550	43.80	33.91	41.68	38.15
-1.7°	700	46.86	31.79	45.45	35.09
+1.7°	150	127.40	26.61	127.63	27.08
+1.7°	550	95.84	29.67	87.83	30.38
+1.7°	700	97.25	31.79	90.90	32.03

TABLE XVI. Pixel functions for 36 μm pixel retrieved from ICU measurements performed during the ground calibration and NECP.

VII. EVOLUTION AFTER LAUNCH

The first flight acquisitions were acquired two months after the JUICE launch on April 2023 during the Near-Earth Commissioning Phase (NECP) that encompassed the initial operations of all instruments on the spacecraft. For MAJIS, a set of full functional tests have been run including a sequence of measurements with the ICU. The ICU uses two light sources, a Quartz Tungsten Halogen (QTH) lamp and a black body illuminating a diffusive target so as to cover the full FOV of MAJIS[14]. This internal optical system provides reference signals necessary to perform in-flight calibration sequences with the QTH optimized for the VISNIR spectral range and the black body for the IR spectral range. The two sources are equipped with a transmission filter exhibiting spectral absorptions that can be used as a reference for monitoring the instrumental spectral response along the mission[14]. We present in the next sub-sections the analysis of the ICU sequences acquired during the NECP that are compared with the same sequences acquired during the ground calibration. During the NECP acquisitions, the OH temperature was 133.5 K, a temperature intermediate between that for the calibration acquisitions (126 K and 137K)

A. Pixel Function

When there is little or no stray light, the evolution of the signal at both edges of the slit can be modeled based on a Gaussian-shaped function, as shown previously (section III A). For a given spectel, the resulting best fit FWHM at the physical pixel level (18 μm) is very similar during calibration and post-launch, indicating that the spatial resolution has remained the same (Table XVI).

B. Channels cross-alignment

The comparison of ICU acquisitions performed after launch (Near Earth Commissioning phase) with that performed during calibration showed that there was a shift in the position of both FOVs, most likely due to launch vibrations. As shown in Fig. 10, the left edge of the VISNIR FOV moved to the right by ≈3.7 pixels and the left edge of the IR FOV moved to the left by ≈2.3 pixels As discussed in Section III C, the start row of the acquisition window can be selected by TC independently for the VISNIR and IR channels. Due to the slight tilt of the detector, there is a small shift of FOV shifts with wavelength (by ≈2 pixels for the VISNIR channel). Therefore, it is best to select the read-out window on the basis of the FOV as observed from the central wavelength (spectel 512), which leads to a positioning of the read-out window from rows 100 to 899 for the VISNIR channel and from row 87 to row 886 for the IR channel (see Table XVII).

Channel	VISNIR			IR		
Band	Bottom px number	Top px number	Shift w.r.t ground calibration	Bottom px number	Top px number	Shift w.r.t ground calibration
150	99.66	897.23	3.98	87.89	888.85	-2.35
550	100.43	899.31	3.81	86.86	888.28	-2.32
700	100.62	899.33	3.78	86.51	887.96	-2.31

TABLE XVII. Position of the start and end rows derived from the ICU acquisitions obtained during the NECP.

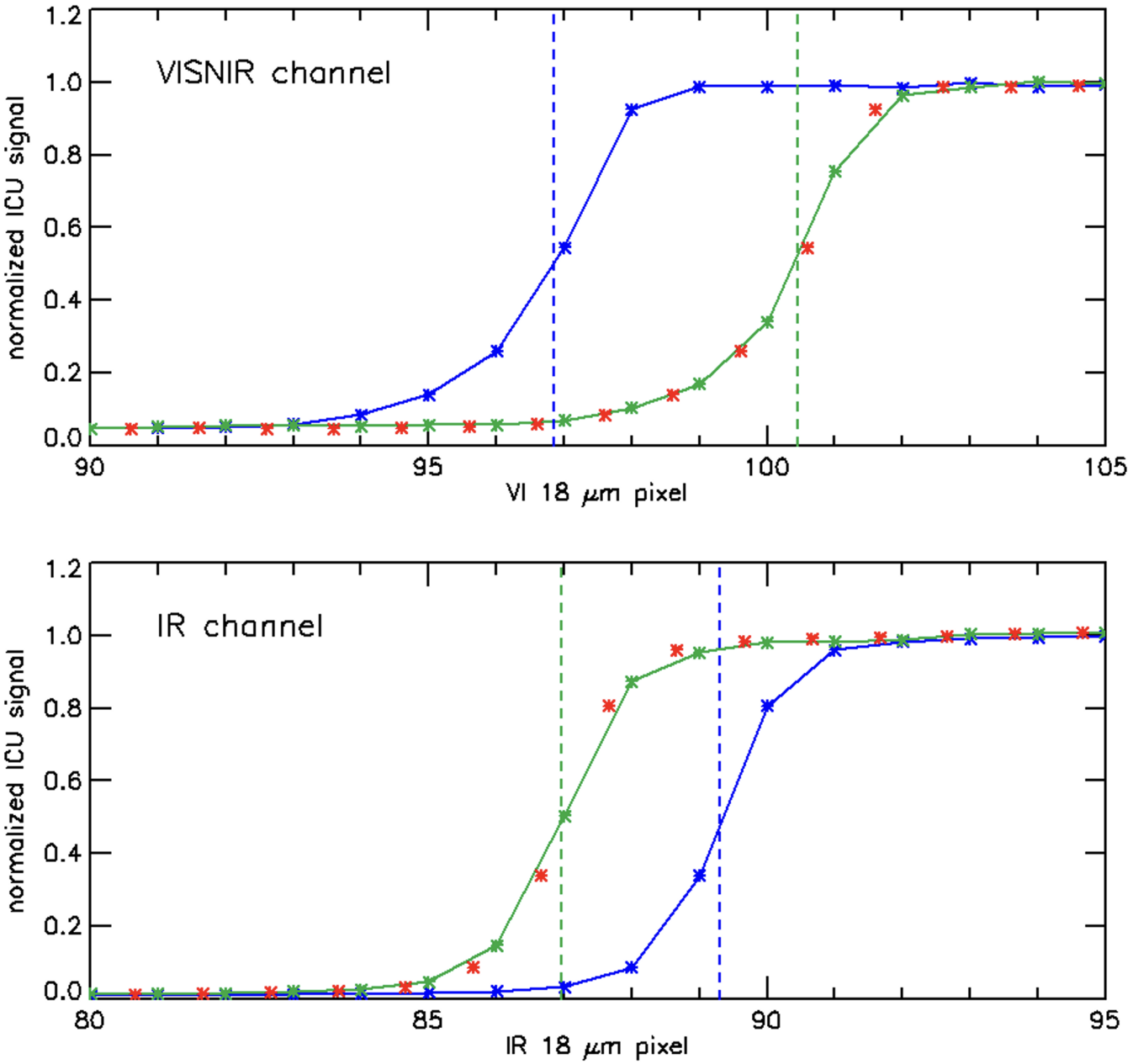

FIG. 10. Signal of the ICU lamp at the left edge of the FOV for the VISNIR channel (top panel) and the IR channel (bottom panel) in the middle of the spectral range (spectel 512). The blue line profile is the one obtained during calibration. The green line profile is the one obtained after launch. The dashed lines correspond to the best estimate of the 50% level before and after launch. The red stars correspond to the profile before launch shifted to the right by 3.7 pixels (VISNIR) and shifted to the left by 2.3 pixels (IR).

VIII. CONCLUSIONS

The spatial response of the MAJIS instrument has been characterized on different positions across the field of view, at different wavelengths, and within the range of expected operative temperatures. The analyses show a substantial compliance between the measured performances and the scientific requirements, as summarised in Table XVIII. Further improvements will be possible in the near future thanks to stellar observations planned during the cruise phase which will allow us to check the evolution of the instrument's spatial response in flight conditions.

	VISNIR channel	IR channel
Datasets, OH temperatures	LDO (T_{OH}=130 K) and IAS (T_{OH}=126-137 K) campaigns	
FOV	100 $\leq$ samples $\leq$ 899	87 $\leq$ samples $\leq$ 886
Fov	$\leq$ 2 physical pixels	
Rotation angle	$\leq$ 2 physical pixels	
Co-registration along slit	-5 (resp. -7.5) physical px from VI to IR channel for b=150 (resp. b=700) using ground measurements -12 (resp. -14) physical px from VI to IR channel for b=150 (resp. b=700) using NECP measurements	
FWHM along slit (36 μm)	52-72 μm at on-axis position 44-50 μm on FOV left edge 52-113 μm on FOV right edge	52-54 μm at on-axis position 40-43 μm on FOV left edge 36-40 μm on FOV right edge
FWHM across slit (36 μm)	55-60 μm at on-axis position 45-50 μm at FOV=$\pm$1.5° positions	45-60 μm at on-axis position 45-55 μm at FOV=$\pm$1.5° positions
Deviation due to OH temperature	FHWM across-slit=50-55 μm on-axis T_{OH}=110-150 K FHWM along-slit=N.A. for non-nominal T_{OH}	FHWM across-slit=50-55 μm for on-axis, T_{OH}=110 K FHWM across-slit=60-75 μm on-axis, T_{OH}=150 K FHWM along-slit=N.A. for non-nominal T_{OH}
Keystone	None	up to 1.4 px for 36 μm pixel

TABLE XVIII. Summary of MAJIS spatial response performances.

IX. ACKNOWLEDGEMENTS

Italian contribution to MAJIS has been coordinated and funded by Italian Space Agency – CONTRACT N. 2021-18-I.0 and supported by the ASI-INAF agreement n. 2023-6-HH.0. French contribution to MAJIS has been technically supported and funded by CNES – CONTRACT CNES – CNRS N. 180 117. The authors acknowledge technical and logistic support from Leonardo Company (Campi di Bisenzio, Florence, Italy), prime industrial contractor of the MAJIS Optical Head. This research has made use of NASA's Astrophysics Data System.

X. CONFLICT OF INTEREST

The authors have no conflicts to disclose.

XI. AUTHOR CONTRIBUTIONS

Alessandra Barbis: formal analysis (supporting); investigation (equal); resources (equal). John Carter: conceptualization (equal); funding acquisition (equal); investigation (equal); resources (equal). Simone De Angelis: conceptualization (equal). Cydalise Dumesnil: data curation (equal); project administration (equal); resources (equal). Gianrico Filacchione: conceptualization (equal); formal analysis (lead); investigation (equal); methodology (lead); writing – original draft (lead). Irene Guerri: conceptualization (equal); investigation (equal). Paolo Haffoud: formal analysis (equal); investigation (equal); methodology (equal); writing – original draft (equal). Yves Langevin: conceptualization (equal); formal analysis (equal); funding acquisition (equal); methodology (supporting); supervision (supporting). Giuseppe Piccioni: conceptualization (equal); funding acquisition (equal); supervision (supporting). Cédric Pilorget: investigation (equal); resources (equal). François Poulet: conceptualization (equal); data curation (equal); funding acquisition (equal); methodology (supporting); project administration (equal); supervision (lead); writing – original draft (supporting). Sébastien Rodriguez: investigation (equal); methodology (supporting). Stefania Stefani: investigation (equal); resources (equal). Leonardo Tommasi: conceptualization (equal); investigation (equal); resources (equal); supervision (supporting). Federico Tosi: conceptualization (supporting). Mathieu Vincendon: conceptualization (equal); data curation (equal); methodology (supporting); project administration (equal); supervision (lead); writing – original draft (supporting).

XII. DATA AVAILABILITY

The data that support the findings of this study are available from the corresponding author upon reasonable request.

[1] Alberto Adriani, Gianrico Filacchione, Tatiana Di Iorio, Diego Turrini, Raffaella Noschese, Andrea Cicchetti, Davide Grassi, Alessandro Mura, Giuseppe Sindoni, Massimo Zambelli, Giuseppe Piccioni, Maria T. Capria, Federico Tosi, Roberto Orosei, Bianca M. Dinelli, Maria L. Moriconi, Elio Roncon, Jonathan I. Lunine, Heidi N. Becker, Alessadro Bini, Alessandra Barbis, Luciano Calamai, Claudio Pasqui, Stefano Nencioni, Maurizio Rossi, Marco Lastri, Roberto Formaro, and Angelo Olivieri. JIRAM, the Jovian Infrared Auroral Mapper. *Space Science Reviews*, 213(1-4):393–446, November 2017.

[2] E. Ammannito, G. Filacchione, A. Coradini, F. Capaccioni, G. Piccioni, M. C. de Sanctis, M. Dami, and A. Barbis. On-ground characterization of Rosetta/VIRTIS-M. I. Spectral and geometrical calibrations. *Review of Scientific Instruments*, 77(9):093109–093109, September 2006.

[3] A. Barbis, M. Barilli, A. Bini, M. Dami, E. Fossati, G. Pilato, L. Tommasi, G. Filacchione, S. De Angelis, G. Piccioni, S. Stefani, F. Tosi, C. Dumesnil, P. Haffoud, Y. Langevin, M. Amoroso, R. Mugnuolo, and F. Poulet. MAJIS/JUICE optical head: characterization campaign and derived performance test results. In Laura E. Coyle, Shuji Matsuura, and Marshall D. Perrin, editors, *Space Telescopes and Instrumentation 2022: Optical, Infrared, and Millimeter Wave*, volume 12180 of *Society of Photo-Optical Instrumentation Engineers (SPIE) Conference Series*, page 121800G, August 2022.

[4] John Carter, Paolo Haffoud, Yves Langevin, François Poulet, Christian Ketchazo, Pierre Guiot, Cydalise Dumesnil, Claudia Ruiz de Galarreta Fanjul, Antoine Arondel, Vincent Carlier, Jean-Pierre Dubois, Ludovic Gonnod, Cyrille Hannou, Véronique Hervier, Jean-Christophe Le Clec'h, Benoit Lecomte, Gilles Morinaud, and Xueyan Zhang. MAJIS IR channel: 3) performance of the focal plane unit. In Laura E. Coyle, Shuji Matsuura, and Marshall D. Perrin, editors, *Space Telescopes and Instrumentation 2022: Optical, Infrared, and Millimeter Wave*, volume 12180 of *Society of Photo-Optical Instrumentation Engineers (SPIE) Conference Series*, page 121803A, August 2022.

[5] Gianrico Filacchione, Fabrizio Capaccioni, Francesca Altieri, Cristian Carli, Iacopo Ficai Veltroni, Michele Dami, Leonardo Tommasi, Gianluca Aroldi, Donato Borrelli, Alessandra Barbis, Marco Baroni, Guia Pastorini, and Raffaele Mugnuolo. The pre-launch characterization of SIMBIO-SYS/VIHI imaging spectrometer for the BepiColombo mission to Mercury. I. Linearity, radiometry, and geometry calibrations. *Review of Scientific Instruments*, 88(9):094502, September 2017.

[6] I. Guerri, A. Fabbri, L. Tommasi, A. Taiti, M. Amoroso, R. Mugnuolo, G. Filacchione, S. Fonti, G. Piccioni, B. Saggin, F. Tosi, and M. Zambelli. The optical design of the MAJIS instrument on board of the JUICE mission. In Laurent Mazuray, Rolf Wartmann, and Andrew P. Wood, editors, *Optical Design and Engineering VII*, volume 10690 of *Society of Photo-Optical Instrumentation Engineers (SPIE) Conference Series*, June 2018.

[7] Paolo Haffoud, Antoine Arondel, David Bolsée, Vincent Carlier, John Carter, Miriam Cisneros-González, Jean-Pierre Dubois, Cydalise Dumesnil, Gianrico Filacchione, Ludovic Gonnod, Cyrille Hannou, Véronique Hervier, Özgür Karatekin, Christian Ketchazo, Yves Langevin, Jean-Christophe Le Clec'h, Benoit Lecomte, Gilles Morinaud, Nuno Pereira, Giuseppe Piccioni, Ann-Carine Vandaele, Lionel Van Laeken, Mathieu Vincendon, and Francois Poulet. MAJIS VIS-NIR channel: performances of the focal plane unit - flight model. In Laura E. Coyle, Shuji Matsuura, and Marshall D. Perrin, editors, *Space Telescopes and Instrumentation 2022: Optical, Infrared, and Millimeter Wave*, volume 12180 of *Society of Photo-Optical Instrumentation Engineers (SPIE) Conference Series*, page 1218039, August 2022.

[8] Paolo Haffoud and etal. Calibration of majis (moons and jupiter imaging spectrometer): Iii. spectral calibration. *Rev. Sci. Instr., submitted*, 2024.

[9] Yves Langevin, Vincent Carlier, Cyrille Hannou, Ludovic Gonnod, John Carter, Federico Tosi, Gianrico Filacchione, Cydalise Dumesnil, G. Piccioni, and François Poulet. H1RG readout procedures for MAJIS, the VIS/NIR imaging spectrometer of JUICE: impacts on the performances. In Laura E. Coyle, Shuji Matsuura, and Marshall D. Perrin, editors, *Space Telescopes and Instrumentation 2022: Optical, Infrared, and Millimeter Wave*, volume 12180 of *Society of Photo-Optical Instrumentation Engineers (SPIE) Conference Series*, page 1218037, August 2022.

[10] Yves Langevin and etal. Calibration of majis (moons and jupiter imaging spectrometer): Iv. radiometric calibration. *Rev. Sci. Instr., submitted*, 2024.

[11] Nuno Pereira, Miriam E. Cisneros-González, David Bolsée, Lionel Van Laeken, Ann C. Vandaele, Samuel Gissot, Yves Langevin, Paolo Haffoud, and François Poulet. MAJIS VIS-NIR channel: performances of the spare model focal plane unit. In Laura E. Coyle, Shuji Matsuura, and Marshall D. Perrin, editors, *Space Telescopes and Instrumentation 2022: Optical, Infrared, and Millimeter Wave*, volume 12180 of *Society of Photo-Optical Instrumentation Engineers (SPIE) Conference Series*, page 121803I, August 2022.

[12] François Poulet, Giuseppe Piccioni, Yves Langevin, Cydalise Dumesnil, Leonardo Tommasi, Vincent Carlier, Gianrico Filacchione, and etal. Moons and jupiter imaging spectrometer (majis) on jupiter icy moons explorer (juice). *SSR*, submitted.

[13] S. Rodriguez and etal. Calibration of majis (moons and jupiter imaging spectrometer): V. observations of representative samples during the majis calibration. *Rev. Sci. Instr., in preparation*, 2024.

[14] S. Stefani and etal. Calibration of majis (moons and jupiter imaging spectrometer): Vi. the internal calibration unit (icu). *Rev. Sci. Instr. (in prepration)*, 2024.

[15] Anne Thorne, Ulf Litzen, and Sveneric Johansson. *Spectrophysics*. Springer, 1999.

[16] M. Vincedon and etal. Calibration of majis (moons and jupiter imaging spectrometer): I. calibration set-up. *Rev. Sci. Instr., in preparation*, 2024.

[17] Naoto Yokoya, Norihide Miyamura, and Akira Iwasaki. Detection and correction of spectral and spatial misregistrations for hyperspectral data using phase correlation method. *Applied Optics*, 49(24):4568, August 2010.